Front. Energy
https://doi.org/10.1007/s11708-024-0948-2

RESEARCH ARTICLE

# Pyrochlore $La_2Zr_{2-x}Ni_xO_7$ anodes for direct ammonia solid oxide fuel cells

**Shiqing Yang, Yijie Gao, Xinmin Wang, Fulan Zhong (✉), Huihuang Fang, Yu Luo (✉), Lilong Jiang**

National Engineering Research Center of Chemical Fertilizer Catalyst (NERC-CFC),
College of Chemical Engineering, Fuzhou University, Fuzhou 350002, China

**Abstract** Developing efficient anode catalysts for direct ammonia solid oxide fuel cells ($NH_3$-SOFCs) under intermediate-temperatures is of great importance, in support of hydrogen economy via ammonia utilization. In the present work, the pyrochlore-type $La_2Zr_{2-x}Ni_xO_{7+\delta}$ (LZN$_x$, $x$ = 0, 0.02, 0.05, 0.08, 0.10) oxides were synthesized as potential anode catalysts of $NH_3$-SOFCs due to the abundant Frankel defect that contributes to the good conductivity and oxygen ion mobility capacity. The effects of different content of $Ni^{2+}$ doping on the crystal structure, surface morphology, thermal matching with YSZ (Yttria-stabilized zirconia), conductivity, and electrochemical performance of pyrochlore oxides were examined using different characterization techniques. The findings indicate that the LZN$_x$ oxide behaves as an n-type semiconductor and exhibits an excellent high-temperature chemical compatibility and thermal matching with the YSZ electrolyte. Furthermore, LZN$_{0.05}$ exhibits the smallest conductive band potential and bandgap, making it have a higher power density as anode material for $NH_3$-SOFCs compared to other anodes. As a result, the maximum power density of the LZN$_{0.05}$-40YSZ composite anode reaches 100.86 mW/cm$^2$ at 800 °C, which is 1.8 times greater than that of NiO-based $NH_3$-SOFCs (56.75 mW/cm$^2$) under identical flow rate and temperature conditions. The extended durability indicates that the $NH_3$-SOFCs utilizing the LZN$_{0.05}$-40YSZ composite anode exhibits a negligible voltage degradation following uninterrupted operation at 800 °C for 100 h.

**Keywords** anode catalyst, ammonia oxidation, Ni particles, $NH_3$-SOFCs

## 1 Introduction

The increased demand for electricity inevitably leads to significant fossil fuel consumption and greenhouse gas emissions [1–5]. Solid oxide fuel cell (SOFC) is a highly efficient electrochemical power generation device that utilizes fuels like hydrogen ($H_2$) and hydrocarbons to achieve high power density energy conversion [6–12]. $H_2$ is considered as the clean fuel of the future due to the absence of carbon emissions [11,13]. However, the storage and transportation of $H_2$, which has a low bulk density and boiling point, becomes a major obstacle for large-scale applications [14,15]. In recent years, ammonia ($NH_3$) is emerging as a preferred hydrogen-rich carrier due to its high hydrogen content, high energy density, non-carbon content, and easy liquefaction [16–18]. The synthesis and utilization of green ammonia is shown in Fig. 1. $NH_3$ undergoes electrochemical oxidation at the anode via reforming reactions, and the enthalpy change of the reforming reactions is considerably less than that of hydrocarbons (e.g., $CH_4$) [19,20]. Therefore, $NH_3$ can be utilized directly as fuel for SOFCs even at reduced temperatures (below 773 K). Several researchers have used Ni/YSZ anode in direct ammonia SOFCs ($NH_3$-SOFCs) [21], but with a performance of only about 88 mW/cm$^2$ at 800 °C. Hence, optimizing the performance of $NH_3$-SOFCs at low-medium temperatures is a matter of interest. Since the anode plays a pivotal role in the electrochemical oxidation of $NH_3$, the selection of anode catalyst can significantly impact the performance of $NH_3$-SOFCs.

Currently, researchers have explored various anode catalysts with different structures for SOFCs, including fluorite, rutile, spinel, perovskite, and double perovskite. The main metal-fluorite ceramic electrodes are Ni/YSZ, SDC (Sm-doped ceria), and Ni/SSZ (Sc-stabilized

---

Received Mar. 12, 2024; accepted Apr. 29, 2024; online Jun. 1, 2024

Correspondences: Fulan Zhong, zhongfulan@fzu.edu.cn;
Yu Luo, luoy@fzu.edu.cn

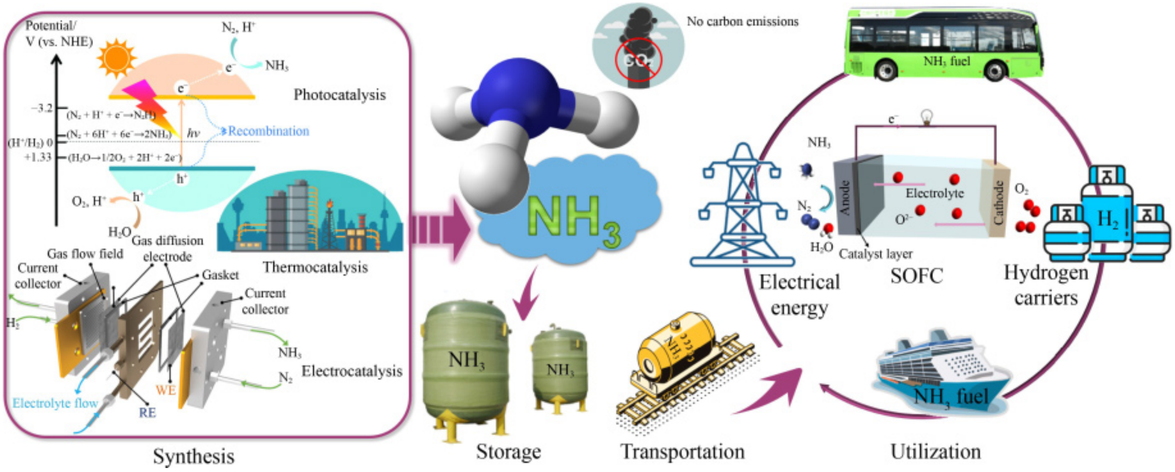

**Fig. 1** Synthesis and utilization of green ammonia.

zirconia), of which, Ni/YSZ is considered to be the maturest anode catalyst, attributed to its superior catalytic activity for fuel gas and good electrical conductivity [22,23]. However, Ni/YSZ ceramic anode has a poor redox stability and a weak tolerance to trace $H_2S$ in fuel gas [24]. Additionally, the $NH_3$ oxidation activity of conventional Ni/YSZ ceramic anode decreases at around 700 °C. At temperatures below 700 °C, the agglomeration of Ni-based catalysts results in a degradation of the anode performance [25]. Therefore, there is an urgent need to find other alternative anode catalyst. Perovskite oxides ($ABO_3$) are considered to have a better stability and have been used in the SOFCs field. However, the electrical conductivity and inherent catalytic activity of these materials are relatively low.

Pyrochlore oxides have attracted considerable interest owing to their outstanding chemical and physical structural stability, high conductivity, and the ability to facilitate oxygen ion mobility. The distinctive and porous structure of the pyrochlore oxide allows the accommodation of oxygen ions in the vacancy, leading to the formation of Frankel defects and the generation of ionic conductivity, which is characterized by an intrinsic oxygen vacancy rate of 12.5%. In addition, doping other ions will also improve the hole concentration to enhance the conductivity of material. Holtappels and Böhm [26] found that after replacing the $Sn^{4+}$ element in $Pr_2Sn_2O_7$ with 5% $In^{3+}$ at 1000 °C, the conductivity increased from $9\times10^{-5}$ to $6.5\times10^{-3}$ S/cm. It is widely recognized that the sturdiness of the pyrochlore structure is primarily determined by the proportion of ionic radii between A-site and B-site cations, with the necessary range for the ratio of $r(A^{3+})/r(B^{4+})$ falling from 1.46 to 1.78 [27,28]. Rare earth zirconates within pyrochlore oxides demonstrate a higher ionic conductivity and stability than rare earth stannates in high-temperature phases. As temperature rises, certain rare earth zirconates may transition from a well-ordered pyrochlore configuration into a chaotic defect fluorite arrangement [29,30]. For instance, the transition temperatures for $Nd_2Zr_2O_7$, $Sm_2Zr_2O_7$, and $Gd_2Zr_2O_7$ are 2573, 2273, and 1803 K, respectively, while $La_2Zr_2O_7$ maintains its organized pyrochlore structure from room temperature to its melting point due to larger ionic radius among rare earth ions.

The present work focuses on the preparation of pyrochlore structure $La_2Zr_{2-x}Ni_xO_7$ (LZN$_x$, $x$ = 0, 0.02, 0.05, 0.08, 0.10) oxides as anodes by sol-gel process. It examines the impacts of varying $Ni^{2+}$ doping levels on the crystal structure, surface morphology, thermal compatibility with YSZ, electrical conductivity, and electrochemical performance of pyrochlore using XRD, Raman, SEM, TEC, Mott-Schottky, UV-Vis DRS, and conductivity tests. The findings indicate that LZN$_x$ oxide behaves as an n-type semiconductor, displaying an excellent high-temperature chemical compatibility and thermal matching with the YSZ electrolyte. Furthermore, LZN$_{0.05}$ exhibits the smallest conductive band potential ($E_{CB}$) and bandgap, making it have a higher power density as anode material for $NH_3$-SOFCs compared to other anodes.

## 2 Experiment

### 2.1 Preparation of $La_2Zr_{2-x}Ni_xO_{7+\delta}$ oxides

Pyrochlore $La_2Zr_{2-x}Ni_xO_{7+\delta}$ (LZN$_x$, $x$ = 0, 0.02, 0.05, 0.08, 0.10) oxides were synthesized using the sol-gel method. First, the raw materials of $Ni(NO_3)_2\cdot6H_2O$, $La(NO_3)_3\cdot6H_2O$, $Zr(NO_3)_4\cdot5H_2O$ along with citric acid were weighed according to the appropriate stoichiometric ratios and dissolved in a large beaker. Then, the mixed clear solution was placed and stirred at 85 °C for 4 h for evaporation to finally form the gel. Afterwards, the gel was dried in a high temperature blast oven at 120 °C for

8 h, producing a sparsely porous material. Finally, the precursor powder underwent calcination 1200 °C in an air atmosphere for 2 h to obtain a series of target $LZN_x$ powders.

### 2.2 Construction of single cell

To reduce the interference of electrolytes during the preparation of single cells, the SOFCs button cells were prepared using commercial YSZ electrolyte sheets. The MNMO-YSZ composite cathode slurry was obtained by mixing the $Mg_{0.4}Ni_{1.4}Mn_{1.2}O_{4+\delta}$ (MNMO) powder with the YSZ powder at a mass ratio of 2:3 while ball milling for 12 h with a certain amount of pine oil alcohol (dispersant) and ethyl cellulose (binder). The as-prepared MNMO-YSZ cathode slurry was applied to one side of YSZ ($d$ = 5 mm) using the screen printing technique, followed by calcination at 1100 °C for 2 h to obtain electrolyte-supported half-cells with cathodes. Similarly, $LZN_x$ and YSZ powders (3:2 mass ratio) were weighed and ball-milled for 12 h to obtain the $LZN_x$-YSZ composite anode slurry that was coated at the symmetric position of the cathode on the YSZ electrolyte using the same method. The $LZN_x$-40YSZ|YSZ|MNMO-60YSZ single cell obtained was calcined at 1200 °C for 2 h. The YSZ electrolyte with a diameter of 25 mm was chosen as the support sheet of the symmetric cells. The $LZN_x$-YSZ composite anode slurry was first printed on one side of the support sheet ($d$ = 10 mm) using the screen printing technology. After drying at 120 °C for 3 h, the same composite anode slurry was printed on the opposite side with the same size using the same method. After drying at 120 °C for 3 h, it was calcined at 1200 °C for 2 h to obtain the symmetric cells. In this experiment, the fuel cell was evaluated at temperatures ranging from 600 to 800 °C, with increments of 50 °C.

### 2.3 Characterization and measurement

The crystallinity of $LZN_x$ was analyzed by powder X-ray diffractometry (XRD, PANalytical X'Pert instrument using CuKα radiation). The patterns were acquired with a stroke rate of 4 (°)/min scanning in the $2\theta$ range of 10°–80°. The surface elemental valence of $LZN_x$ was examined using X-ray photoelectron spectroscopy (XPS, Thermo Scientific ESCALAB 250 spectrometer), calibrated at C 1s (284.8 eV) for all elemental binding energies. The relative content of oxygen vacancies in $LZN_x$ samples was studied through electron paramagnetic resonance (EPR) detection to identify the existence of unpaired electrons. The particle dimensions and surface characteristics of $LZN_x$ materials were examined by field emission scanning electron microscopy (SEM, Hitachi S-4800 instrument). The conductance of the $LZN_x$ anode material was quantified from 500 to 800 °C using a four-probe DC method by a Keithley 2400 source meter. The thermal expansion coefficient (TEC) was measured using a dilatometer (DIL402C/4/G). The electrochemical performance of the $NH_3$-SOFCs with $LZN_x$ as anode was tested by the Zahner IM6 electrochemical workstation, including the current–voltage ($I$–$V$) curves and electrochemical impedance spectroscopy (EIS).

## 3 Result and discussion

### 3.1 Structural characterization of $LZN_x$

The crystalline phases of different Ni-doped $LZN_x$ oxides are characterized by XRD after calcination at 1200 °C for 2 h, as depicted in Fig. S1(a). The diffraction peaks of all samples match the standard card PDF#73-0444, indicating the absence of impurity phases. This suggests that the fundamental crystal configuration of $La_2Zr_2O_7$ remains unchanged when Ni is doped at a low level. In addition to the diffraction peaks shared by the pyrochlore and fluorite facies at the (222), (400), (440), and (622) crystal planes, the unique superlattice diffraction peaks of pyrochlore also appear at the (111), (311), (331), (511), and (531) crystal planes. These findings indicate that the $LZN_x$ oxides synthesized are all pyrochlore oxides. In the magnified XRD spectrum of the (222) crystal plane, the diffraction peak gradually shifts rightward with increasing Ni doping. This shift may be attributed to the smaller ionic radius of $Ni^{2+}$ (0.069 nm) compared to $Zr^{4+}$ (0.072 nm). The incorporation of Ni with a smaller ionic radius into $La_2Zr_2O_7$ will cause the lattice volume to shrink and the distance between crystal planes to decrease, resulting in a high-angle shift of the diffraction peak.

To further investigate the structural characteristics of the $LZN_x$ series samples, Raman spectroscopy was conducted on $LZN_x$ powder after calcination at 1200 °C for 2 h (in Fig. S1(b)). In contrast to fluorite structures that exhibit a single Raman activity mode, pyrochlore configuration displays six modes active in Raman spectroscopy ($A_{1g} + E_g + 4F_{2g}$) [31,32]. Within the Ni doping range ($x$ = 0–0.1), four distinct Raman peaks are identified in the Raman spectrum [33,34]. Specifically, the Raman peaks around 300 and 520 $cm^{-1}$ are associated with the $F_{2g}$ vibration mode, corresponding to the modes of the O-La-O bending vibration and the La-O stretching vibration, respectively. The attribution of the Raman peak around 395 $cm^{-1}$ is given to the $E_g$ mode of vibration, which involves La-O extension, Zr-O tension, and O-Zr-O bending. Additionally, the Raman peak at 490 $cm^{-1}$ is associated with the La-O stretch vibration, representing the $A_{1g}$ vibration mode. The Raman activity mode of the pyrochlore phase indicates that the prepared samples have a pyrochlore structure and no other impurities are generated, which is consistent with the XRD results.

### 3.2 Microstructure and compatibility analysis of $LZN_x$

The electrode material is a crucial component of SOFCs, playing a pivotal role in the performance of a single cell. It is essential for the electrode material to possess a certain level of porosity to facilitate the transmission of fuel gas, and exhibit a chemical and thermal compatibility with the electrolyte to prevent any chemical reactions or detachment of the electrode during cell operation. To enhance the observation of the anode material and the cross-section of the cell, a mixture of $LZN_0$ and $LZN_{0.05}$ with YSZ was prepared in a 3:2 mass ratio followed by high-temperature calcination and subsequent analysis using SEM, respectively. The microstructure of the $LZN_0$-40YSZ and Ni-doped $LZN_{0.05}$-40YSZ anode materials is depicted in Figs. 2(a) and 2(b). When Ni is not doped, although the anode material has certain pores, the anode particles are large and unevenly distributed with an obvious stacking and aggregation phenomenon. When the content of Ni doping is $x = 0.05$, it can be seen that the particles are smaller and evenly distributed, and the surface pores of the anode material are sufficient, which is conducive to expanding the three-phase boundary (TPB) and facilitating the diffusion of fuel gas. The fuel gas can fully react with $O^{2-}$ transported from the cathode, reducing the polarization resistance [35], and thus improving the performance of the material. From this, it can be seen that the addition of Ni element is conducive to making the anode material more porous and better meeting the requirements of SOFCs for electrode materials.

To assess the chemical compatibility between the $LZN_x$ anodes and the YSZ electrolyte, a mixture of $LZN_{0.05}$ and YSZ samples in a 1:1 mass ratio is subjected to high-temperature treatment. The compatibility between the two samples is analyzed using XRD, as shown in Fig. 2(c). The XRD results indicate that no new diffraction peaks appear, and the peak positions remain unchanged after calcination, demonstrating a good chemical compatibility between the anode and electrolyte materials.

To examine the thermal compatibility between the electrolyte and the anode material, the TECs of $LZN_x$ samples are analyzed in an air atmosphere, ranging from 30 to 800 °C (in Fig. 2(d)). The thermal expansion rates ($\Delta L/L_0$) of the five samples maintain a consistent linear correlation with temperature, indicating that the thermal expansion coefficient of the $LZN_x$ system is not significantly influenced by temperature variations, thereby ensuring a good stability of the high-temperature phase in these samples. By analyzing the thermal expansion rate $\Delta L/L_0$ with temperature, the average TECs for the five

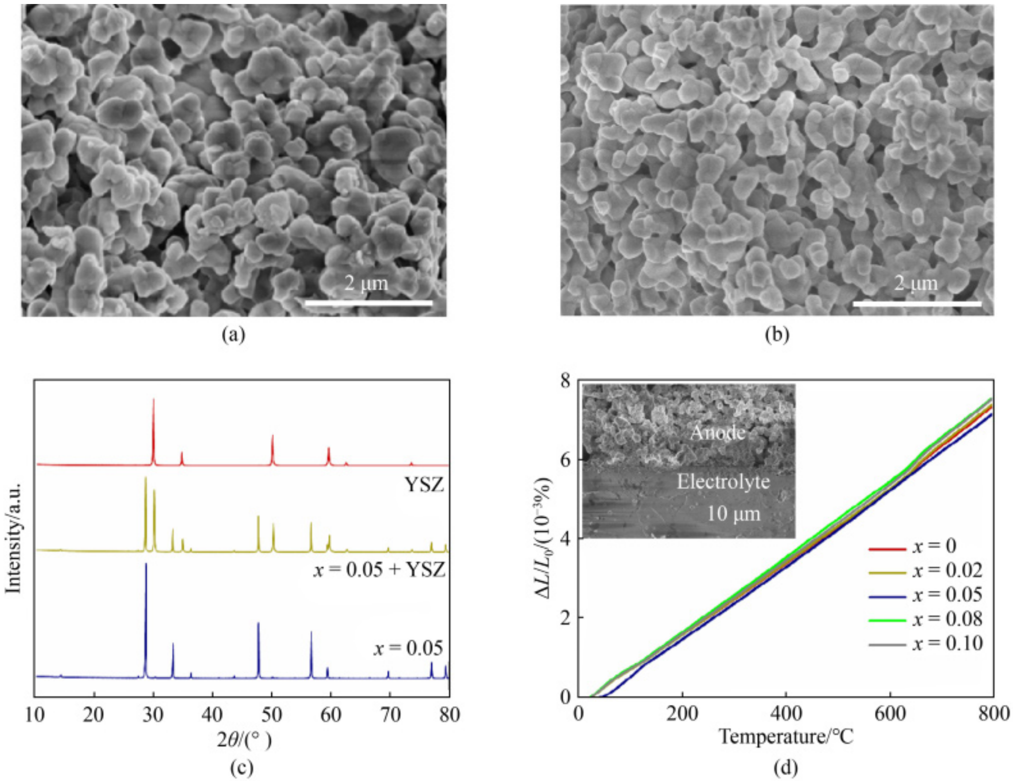

**Fig. 2** Compatibility analysis.

(a) SEM of $LZN_0$-40YSZ; (b) SEM of $LZN_{0.05}$-40YSZ; (c) XRD patterns of $LZN_{0.05}$, YSZ, $LZN_{0.05}$, and YSZ mixed with 1:1 mass ratio; (d) TECs of $LZN_x$ in air (the inset showing the cross-section view of $LZN_{0.05}$ anode after electrochemical reaction).

materials is calculated. The TECs of $LZN_0$, $LZN_{0.02}$, $LZN_{0.05}$, $LZN_{0.08}$, and $LZN_{0.10}$ are $9.16 \times 10^{-6}$, $9.20 \times 10^{-6}$, $9.28 \times 10^{-6}$, $9.42 \times 10^{-6}$, and $9.38 \times 10^{-6}$ $K^{-1}$, respectively. As $x \leqslant 0.08$, the TEC of the material increases with the doping levels. Additionally, when Ni doping is further increased ($x = 0.10$), the TEC of the material begins to decrease. The TEC of the material is related to the lattice structure and crystal bonding energy, and there are two reasons for this phenomenon of $LZN_x$: ① For pyrochlore rare earth zirconate, relevant studies have shown that when the A site rare earth element is the same, the TEC of the material diminishes with the decrease in ionic radius of the B site element [36]. Since the ionic radius of Ni is 0.069 nm, which is smaller than that of Zr (0.072 nm), the increase of Ni will cause the lattice volume to shrink and the crystal plane distance to decrease, so that the lattice energy will increase and TEC will show a downward trend. ② The TEC is affected by the bond energy between atoms. Fan et al. [37] calculated that the B-O bond has a greater effect on the TEC than the La-O and the O-O bonds. Studies have shown when the bond energy of the doped element M-O bond is lower than that of the Zr-O bond, the TEC value of the material will increase [38]. In the present work, the bond energy of the Ni-O bond formed by doping Ni is smaller than that of the Zr-O bond (790 kJ/mol), which leads to an upward trend of TEC. Under the combination of these two effects, the relationship between Ni doping and TEC is not a simple linear one. However, in general, the TEC value of $LZN_x$ system is between $9 \times 10^{-6}$ and $10 \times 10^{-6}$ $K^{-1}$, which is similar to that of YSZ ($10.50 \times 10^{-6}$ $K^{-1}$), indicating that there is a favorable thermal compatibility between the two materials. The illustration in Fig. 2(d) presents a cross-sectional portrayal of the cell. The upper part is made of porous $LZN_{0.05}$-40YSZ anode, which is conducive to the rapid transmission of fuel gas. Contrarily, the lower part is a dense YSZ electrolyte layer, which has no obvious pores or cracks. This is conducive to isolating the fuel gas and oxidation gas well, ensuring that the SOFCs maintain good sealing during operation. After electrochemical reaction, the composite anode material is tightly bonded to the electrolyte without cracks, indicating excellent thermal compatibility between the two materials under high temperature conditions, which aligns with the findings of TEC.

### 3.3 Oxygen vacancy and conductivity analysis of $LZN_x$

The identification and quantification of oxygen vacancies in $LZN_x$ could be assessed through EPR analysis. The EPR spectra of $LZN_x$ series samples are depicted in Fig. 3(a). Oxygen vacancies are identified based on the signal peak at $g = 2.003$, which is the characteristic peak [39]. Furthermore, the intensity of the EPR signal peak can provide insights into the concentration of oxygen vacancies [40]. Therefore, it can be concluded that as the doping amount of Ni element increases, the oxygen vacancies concentration in the oxides correspondingly rises.

The Mott-Schottky curves for $LZN_x$ semiconductor at 500, 1000, and 1500 Hz are shown in Figs. 3(b)–3(f). The semiconductor type of the sample can be preliminarily

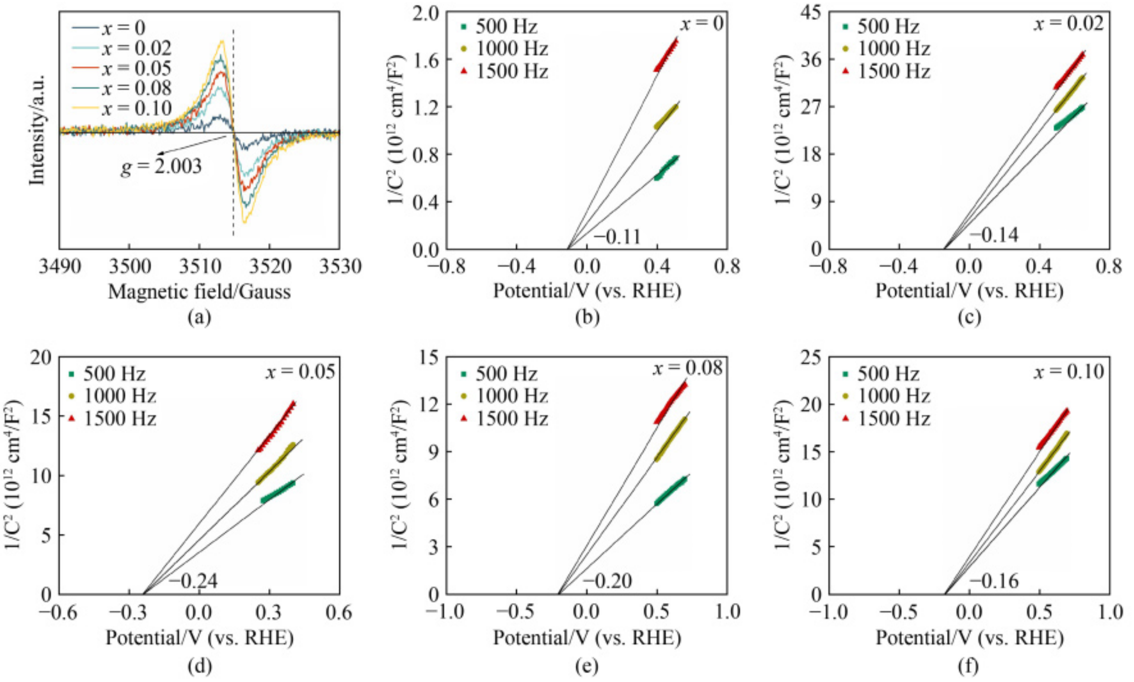

**Fig. 3** Oxygen vacancy and conductivity analysis.
(a) EPR of $LZN_x$; Mott-Schottky curves of (b) $LZN_0$, (c) $LZN_{0.02}$, (d) $LZN_{0.05}$, (e) $LZN_{0.08}$, and (f) $LZN_{0.10}$.

inferred from the slope of the curve. A positive slope signals an n-type semiconductor, whereas a negative slope signifies a p-type semiconductor. In Figs. 3(b)–3(f), the samples of the $LZN_x$ series are all n-type semiconductors [41,42]. The n-type semiconductors are more conducive to catalytic reactions than p-type semiconductors. The Mott-Schottky curves intersect at the $x$-axis, determining the flat band potential ($E_{fb}$) of the sample. In this experiment, the Ag/AgCl electrode is used as a reference electrode for potential measurements, and the Nernst equation is used to convert the potential to that of the standard reversible hydrogen electrode (RHE).

$$E_{RHE} = E_{Ag/AgCl} + 0.059\text{pH} + 0.197, \tag{1}$$

where, the pH value in this test is 7. Figures 3(b)–3(f) reveal that the $E_{fb}$ of $LZN_0$, $LZN_{0.02}$, $LZN_{0.05}$, $LZN_{0.08}$, and $LZN_{0.10}$ oxides is −0.11, −0.14, −0.24, −0.20, and −0.16 V (vs. RHE), respectively. It has been shown in Ref. [43] that for n-type semiconductors, the conduction band potential ($E_{CB}$) is approximately 0.1 V lower than $E_{fb}$. Therefore, it can be concluded that the $E_{CB}$ of $LZN_x$ oxides is −0.21, −0.24, −0.34, −0.30, and −0.26 V (vs. RHE), respectively. With the introduction of Ni, the absolute value of $E_{CB}$ increases first and then decreases, and the absolute value of $E_{CB}$ is the largest when the amount of incorporation $x = 0.05$. This indicates that the reducing ability of the excited electrons on the conduction band is relatively stronger, which is helpful to improve the catalytic activity of semiconductor materials.

Additionally, the conductivity of the semiconductors can be deduced by examining the bandgap width [44]. In general, a smaller bandgap width can enhance the conductivity to some extent. Typically, UV-vis diffuse reflectance spectroscopy is performed on $LZN_x$ oxides, and the absorption spectra are interpreted using the Kubelka-Munk (K-M) formula.

$$F(R_\infty) = \frac{(1-R_\infty)^2}{2R_\infty}, \tag{2}$$

where $R_\infty$ indicates diffuse reflectance. Figure 4(a) reveals typical absorption peaks for all samples within the test range. The bandgap width can be calculated using the Tauc formula [45].

$$\alpha h\nu = A(h\nu - E_g^{\frac{1}{n}}). \tag{3}$$

In this case, $\alpha$ denotes the absorption coefficient, $\nu$ signifies the optical frequency, and $E_g$ indicates the band gap. When the semiconductor undergoes a direct transition, $n$ takes a value of 2, and in an indirect transition, $n$ is equal to 1/2. Plotting $(\alpha h\nu)^n$ with $h\nu$, the linear segment of the curve is extended until it intersects the $x$-axis. The intersection indicates the bandgap width of the semiconductor. In Figs. 4(b)–4(f), the bandgap widths of $LZN_0$, $LZN_{0.02}$, $LZN_{0.05}$, $LZN_{0.08}$, and $LZN_{0.10}$ are 3.75, 3.50, 2.81, 3.00, and 3.27 eV, respectively. With the increase of Ni doping, the bandgap of the five materials decreases first and then increases, and when the doping amount $x = 0.05$, the bandgap of the materials is the smallest. Therefore, it can be inferred that $LZN_{0.05}$ exhibits the highest conductivity. The conductivity test is conducted on the sintered dense $LZN_x$ series cuboid samples at a pure ammonia atmosphere of 400–800 °C (in Fig. 5(a)). The conductivities of $LZN_x$ samples rise in a curve with temperature, which is aligned with the

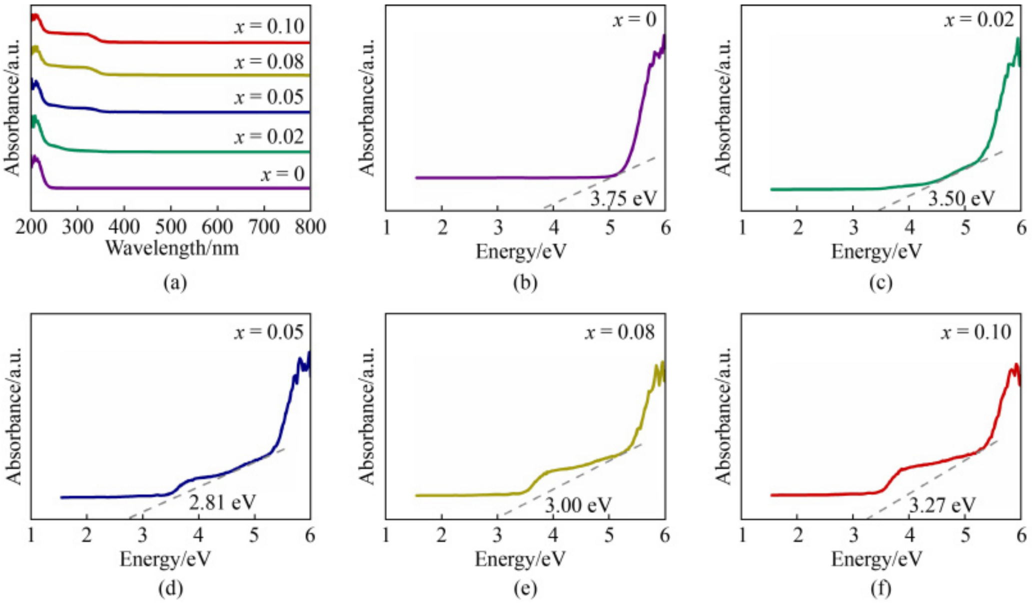

**Fig. 4** UV-vis diffuse reflectance spectroscopy.

(a) Optical absorption spectra for the $LZN_x$; (b) Tauc plot showing the estimated optical bandgap for $LZN_0$, (c) $LZN_{0.02}$, (d) $LZN_{0.05}$, (e) $LZN_{0.08}$, and (f) $LZN_{0.10}$.

conductivity behavior of semiconductor small polarons [46]. As temperature rises from 500 to 650 °C, the conductivity increases slowly with temperature. At 650–800 °C, the conductivity surges swiftly with temperature. The high temperature significantly enhances the conductivity of the sample. The reason for this is that high temperatures increase the migration rate of carriers in the material, which in turn accelerates the diffusion rate of small polarons [47]. According to the equation $\sigma = L/RS$, the conductivity of $LZN_0$, $LZN_{0.02}$, $LZN_{0.05}$, $LZN_{0.08}$, and $LZN_{0.10}$ at 800 °C is $0.42 \times 10^{-5}$, $0.95 \times 10^{-5}$, $5.20 \times 10^{-5}$, $4.26 \times 10^{-5}$, and $3.22 \times 10^{-5}$ S/cm, respectively. It is evident that the conductivity is related to the amount of $Ni^{2+}$ incorporated. As $Ni^{2+}$ concentration rises, the conductivity initially climbs and then falls. The conductivity reaches its peak when the amount is $x = 0.05$, exhibiting an increase of at least 12 times compared to undoped $Ni^{2+}$. This suggests that the appropriate amount of $Ni^{2+}$ doping can significantly enhance the conductivity of $LZN_x$. Through EPR characterization, it is known that Ni doping can gradually raise the oxygen vacancies concentration in $LZN_x$, thereby improving the ion conductivity. However, an excessive presence of oxygen vacancies can impede electron mobility, leading to a reduction in electron conductivity [48]. For doping levels $x \leqslant 0.05$, the rise in ionic conductivity compensates for the decline in electronic conductivity, resulting in an overall increase in conductivity with higher doping levels. Conversely, when $x > 0.05$, the ionic conductivity is insufficient to offset the electronic conductivity, causing a gradual decline in total conductivity. An Arrhenius plot of the conductivity, as depicted in Fig. 5(b), illustrates a linear correlation between $\ln(\sigma T)$ and $1/T$, verifying that the ion conduction of the system is consistent with a thermally activated process.

## 3.4 Electrochemical performance and long-term stability of $LZN_x$ single cells

Based on the above characterization analysis, $H_2$ and $NH_3$ are used as fuel gases and air as oxidation gases. The electrochemical performance of $LZN_x$-40YSZ||YSZ||MNMO-60YSZ cell is tested at a temperature range of 800–600 °C with a temperature interval of 50 °C. In Figs. 6(a) and 6(c), the open-circuit voltage (OCV) of the cell has remained above 1V at different temperatures and fuel atmospheres, indicating that the cell is securely sealed. Figure 6(a) illustrates that the maximum power densities (MPDs) of the prepared cell with $LZN_0$, $LZN_{0.02}$, $LZN_{0.05}$, $LZN_{0.08}$, and $LZN_{0.10}$ as anode are 49.80, 64.11, 100.20, 90.07, and 79.34 mW/cm$^2$ in $H_2$ fuel at 800 °C, respectively. Figure 6(c) shows that the MPDs of the single cells with $LZN_0$, $LZN_{0.02}$, $LZN_{0.05}$, $LZN_{0.08}$, and $LZN_{0.10}$ as anodes in an ammonia atmosphere at 800 °C are 12.29, 53.91, 100.86, 80.17, and 72.16 mW/cm$^2$, respectively. Whether in $H_2$ or $NH_3$ atmosphere, with the increase of the doping amount of $Ni^{2+}$ at the B site, the MPD of the cell increases first and then decreases. When the doping amount of $Ni^{2+}$ is $x = 0.05$, the power density of the cell reaches the maximum value. This can be attributed to the fact that $LZN_{0.05}$ possesses the lowest conduction band potential, the narrowest band gap, and the highest conductivity, resulting in the optimal electrocatalytic activity.

At 800 °C, the $MPD_{(NH_3)}$ of all single cells is lower than that of $MPD_{(H_2)}$, and the $MPD_{(NH_3)}/MPD_{(H_2)}$ ratios of $LZN_0$, $LZN_{0.02}$, $LZN_{0.05}$, $LZN_{0.08}$, and $LZN_{0.10}$ are 25%, 84%, 93%, 89%, and 91%, respectively. It can be seen that the incorporation of $Ni^{2+}$ greatly increases the $MPD_{(NH_3)}/MPD_{(H_2)}$ ratio in single cell, which is attributed to the following two aspects. On the one hand, the impedance value is different at the same temperature.

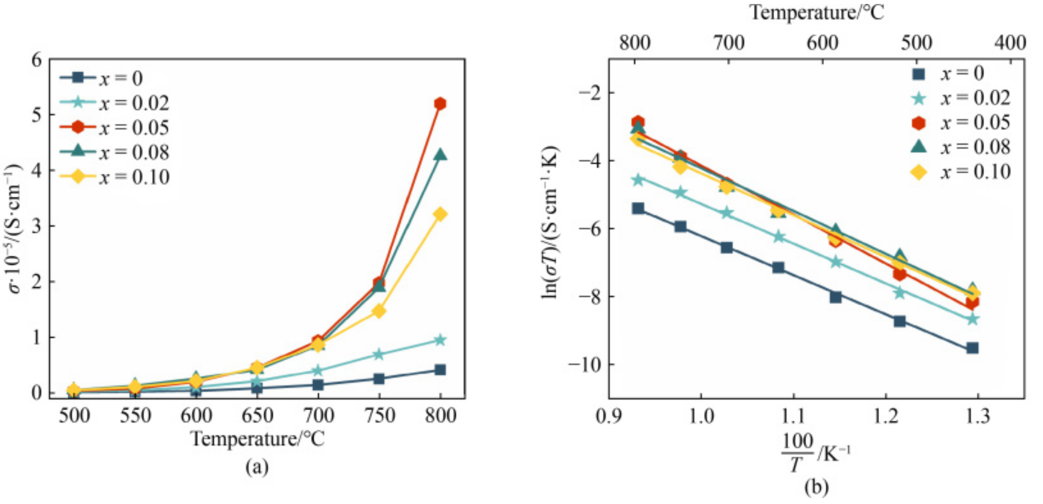

(a)

(b)

**Fig. 5** Electrical conductivity analysis.

(a) Conductivity vs. temperature of $LZN_x$; (b) Arrhenius plot of electrical conductivity of $LZN_x$ samples.

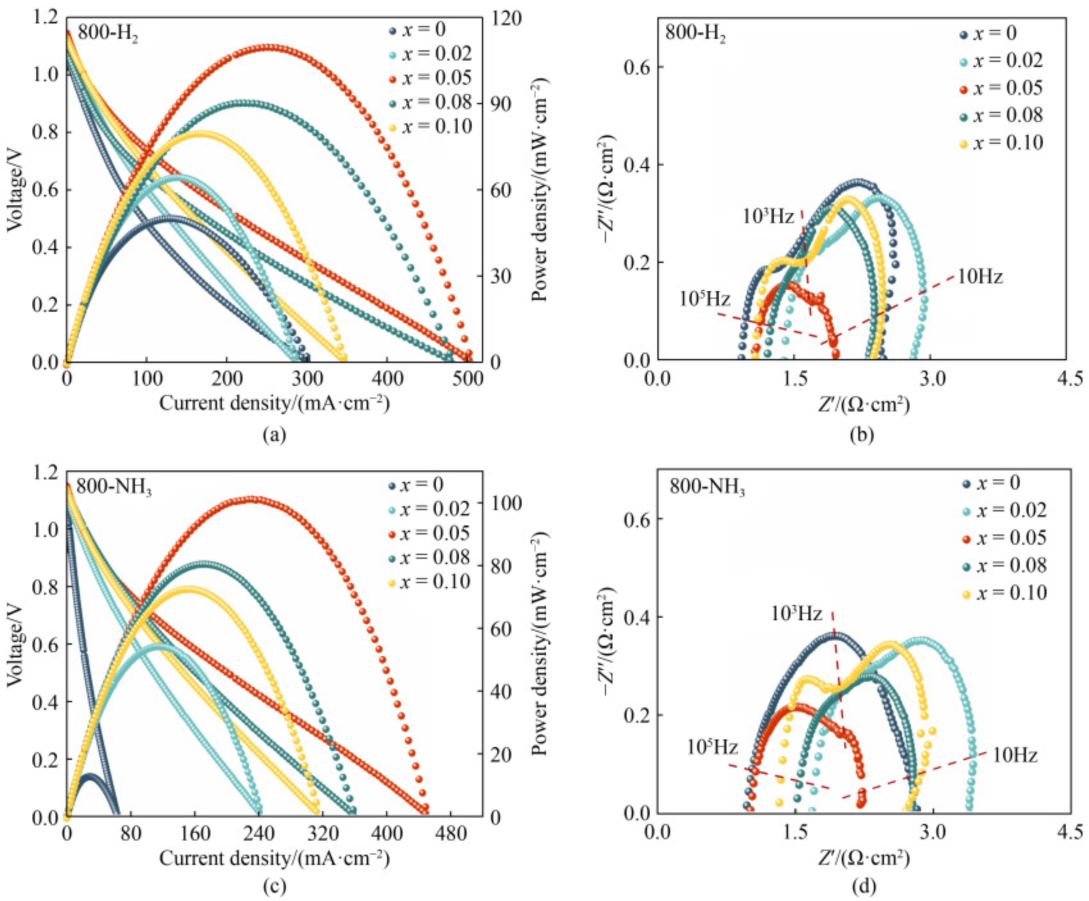

**Fig. 6** Electrochemical activity.

(a) *I–V–P* and (b) EIS of the single cell based on LZN$_x$-40YSZ anode with $H_2$ as fuel; (c) *I–V–P* and (d) EIS of the single cell based on LZN$_x$-40YSZ anode with $NH_3$ as fuel at 800 °C.

Figures 6(b) and 6(d) show the Nyquist plots with LZN$_x$ as the anode material in $H_2$ and $NH_3$ atmosphere at 800 °C, respectively. The intercept value between the high-frequency terminal and the $x$-axis is the ohmic resistance ($R_O$), and the polarization resistance ($R_P$) is calculated by the difference between the intercept of the high-frequency terminal and the low-frequency terminal and the $x$-axis, respectively. As can be obtained from Fig. 6(b), the $R_O$ of the cells using LZN$_0$, LZN$_{0.02}$, LZN$_{0.05}$, LZN$_{0.08}$, and LZN$_{0.10}$ as anode materials is 0.92, 1.40, 1.04, 1.21, and 1.07 Ω·cm$^2$, and the calculated $R_P$ is 1.54, 1.42, 0.93, 1.12, and 1.31 Ω·cm$^2$ in $H_2$ atmosphere at 800 °C, respectively. In $NH_3$ atmosphere, the $R_O$ of the cell is 0.97, 1.68, 1.01, 1.52, and 1.32 Ω·cm$^2$, and the $R_P$ calculated is 1.86, 1.72, 1.21, 1.26, and 1.40 Ω·cm$^2$, respectively. The $R_O$ of the cell varies slightly due to the difference in the thickness of the commercial YSZ electrolyte sheet purchased. At the same temperature and atmosphere, the smaller the $R_P$ of the cell, the better the electrochemical performance, which is consistent with the previous conclusion of Ni$^{2+}$ doping. At identical temperature, the $R_P$ in the $NH_3$ atmosphere is higher than that in $H_2$, which results in a smaller MPD of single cell fueled by $NH_3$.

Another reason is that the reaction path of fuel gas at the anode needs to be explored. The anode reaction pathway accepted is that $NH_3$ initially breaks down into $H_2$ and $N_2$, followed by the reaction of $H_2$ with $O^{2-}$ ions transmitted from the cathode [49]. For this purpose, the ammonia decomposition performance of NiO and LZN$_{0.05}$ is tested and compared at 600–800 °C, as shown in Fig. 7(a). The ammonia decomposition performance of the traditional NiO anode catalyst is greater than that of the LZN$_{0.05}$ anode catalyst, and the ammonia conversion rate of the catalyst in the present work is only 60.20% at 800 °C. Therefore, it can be speculated that in addition to $NH_3$ decomposition, the direct $NH_3$ oxidation can also occur at the anode side. In addition, the reaction pathway of ammonia can also be determined by OCV. Thermodynamically, the standard Gibbs free energies associated with the direct ammonia electrooxidation and $NH_3$ decomposition exhibit distinct temperature dependencies [50]. As shown in Fig. 7(b), when using $H_2$ as the fuel, the OCV of the cell using LZN$_{0.05}$ as anode material is 1.143, 1.158, 1.165, 1.169, and 1.183 V at 800, 750, 700, 650, and 600 °C, respectively. As the temperature

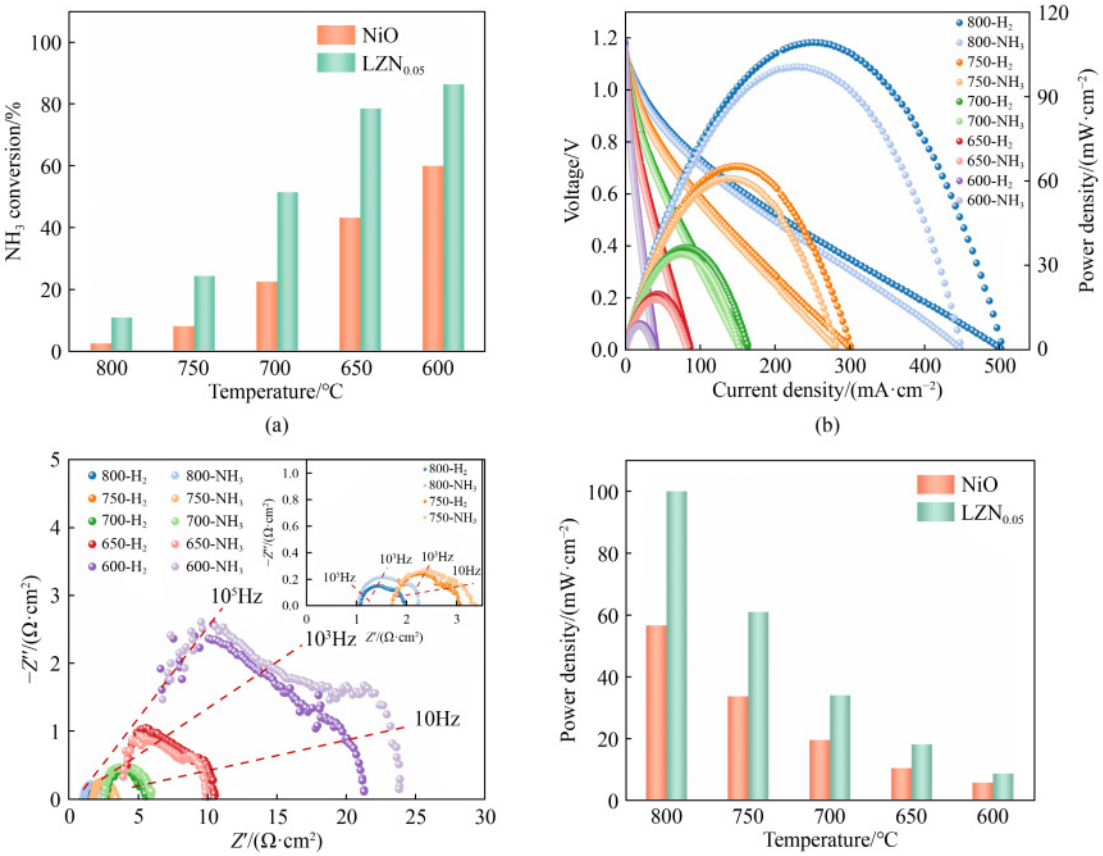

(a) (b)

(c) (d)

**Fig. 7** Ammonia decomposition and electrochemical activity.

(a) Ammonia decomposition activity for NiO and $LZN_{0.05}$ anode catalysts (air velocity of 30000 $mL\cdot(g\cdot h)^{-1}$); (b) *I–V–P*; (c) EIS of the single cell based on $LZN_{0.05}$-40YSZ anode with $H_2$ or $NH_3$ as fuel at 600–800 °C; (d) MPD comparison of the single cell based on $LZN_{0.05}$-40YSZ and NiO-40YSZ anodes using $NH_3$ as fuel at 800 °C.

rises, the OCV value decreases. This phenomenon is consistent with the law that the theoretical potential of hydrogen-oxygen fuel cells changes with temperature [51]. However, the OCV is 1.152, 1.160, 1.165, 1.165, and 1.165 V when $NH_3$ is used as fuel, respectively, which is inconsistent with the fact that the OCV of ammonia direct oxidation should increase with increasing operating temperature. Therefore, it can be speculated that there may be two reaction pathways of direct $NH_3$ and indirect $NH_3$ oxidation reaction pathways in the present work. Based on the above results, it can be concluded that the second reason for the reduction in the MPD of $NH_3$ fuel, compared to that of $H_2$ fuel cell, is that $NH_3$ partially decomposes into $N_2$ and $H_2$, and $N_2$ acts as a dilution to $H_2$ [52], resulting in smaller MPD values.

Figure 7(b) shows the *I–V–P* curves of the cell using $LZN_{0.05}$ as anode material under different fuels in the temperature range of 800–600 °C. The MPD of the cell gradually increases when the temperature increases, because the catalytic activity of $LZN_{0.05}$ increases, thereby enhancing the migration rate of electrons and ions. $MPD_{(NH_3)}$ is smaller than $MPD_{(H_2)}$ under the same temperature conditions, and this difference is mainly due to the fact that the $NH_3$ decomposition reaction absorbs heat and the real temperature of the cell is lower than that recorded by the thermocouple. As a result, the impedance in $NH_3$ at the same temperature will be greater than that in $H_2$ (Fig. 7(c)), resulting in a smaller MPD in $NH_3$-SOFCs. Figure 7(d) compares the MPD of the single cells with NiO and $LZN_{0.05}$ as the anodes in a pure $NH_3$ atmosphere. The performance of the single cell of Ni-YSZ anode in $H_2$ is presented in Fig. S2. $LZN_{0.05}$ has a better performance than NiO. The MPD of $LZN_{0.05}$ is 100.86 $mW/cm^2$ at 800 °C, and the MPD of NiO is only 56.75 $mW/cm^2$, indicating that $LZN_{0.05}$ has a good application potential in SOFCs anode materials.

For a single cell, besides the high MPD, the durability of a single cell under the high temperature condition is also important. Therefore, the long-term stability of $LZN_{0.05}$-40YSZ|YSZ|MNMO-60YSZ electrolyte supported cell is tested in the $NH_3$ atmosphere. As can be seen from Fig. 8, after 100 h of uninterrupted operation with a steady current density of 50 $mA/cm^2$ at 800 °C, there is almost no change in the voltage of the cell, indicating that the single cell has a good long-term stability.

### 3.5 Electrochemical impedance of symmetric cell

EIS can effectively evaluate the electrochemical activity. In this experiment, the ZView software was employed to analyze the $R_b(R_L//CPEL)(R_M//CPEM)(R_H//CPEH)$ equivalent circuit. Figure 9(a) shows the EIS diagram of LZN$_x$-40YSZ|YSZ|LZN$_x$-40YSZ symmetric cell in $NH_3$ at 800 °C with a flow rate of 50 sccm （standard cubic centimeter per minute））. The scattered dots represent the EIS experimental test results, and the solid line denotes the EIS fitting results. $R_b$ indicates the ohmic impedance of the symmetric cell. Since the same diameter (25 mm) of YSZ commercial electrolyte sheet is used in the EIS test, the ohmic resistance during the test is similar to about 1.0 $\Omega\cdot cm^2$, and $R_b$ is normalized to zero in order to compare $R_P$ easily. The $R_P$ of the symmetric cell consists of three parts, i.e., high-frequency impedance ($R_H$), mid-frequency impedance ($R_M$), and low-frequency impedance ($R_L$) [53]. The EIS data are simulated and analyzed by the Matlab software, and the distribution of relaxation time (DRT) curves are shown in Fig. 9(b). The values of $R_H$, $R_M$, and $R_L$ are obtained by integrating the area of different characteristic peaks. Figure 9(c) shows the $R_M$, $R_L$, $R_H$, and $R_P$ values at 800 °C. The $R_P$ values of symmetric cells with LZN$_0$, LZN$_{0.02}$, LZN$_{0.05}$, LZN$_{0.08}$, and LZN$_{0.10}$ as electrodes are 33.04, 32.81, 4.63, 13.30, and 22.10 $\Omega\cdot cm^2$, respectively. The $R_P$ of LZN$_{0.05}$ is significantly lower than that of pure $La_2Zr_2O_7$, indicating that $Ni^{2+}$ doping can effectively decrease the impedance of the material. The rise in $Ni^{2+}$ doping levels is associated with an increase in oxygen vacancy concentration. An appropriate oxygen vacancy concentration is beneficial for enhancing ion diffusivity. However, excessive oxygen vacancy accumulation can impede charge conduction. Consequently, the trend observed in the $R_P$ value is characterized by an initial decrease followed by an increase as Ni doping levels rise. The $R_P$ value shows a good match with the MPD, and the MPD of the single cell increases when the $R_P$ value decreases. By calculation, the $R_L$ of symmetric cells with LZN$_0$, LZN$_{0.02}$, LZN$_{0.05}$, LZN$_{0.08}$, and LZN$_{0.10}$ as electrodes accounts for 65.22%, 50.22%, 45.79%, 45.71%, and 52.04% of $R_P$, $R_M$ for 30.81%, 40.48%, 42.98%, 42.10%, and 38.37% of $R_P$, and $R_H$ for 3.96%, 9.30%, 11.23%, 12.18%, and 9.91%, respectively. In the doping range of $Ni^{2+}$, $R_L$ accounts for a large proportion. $R_L$, $R_M$, and $R_H$ denote distinct reaction mechanisms, which encompass the diffusion of fuel gases and intermediates within the gas phase, the adsorption and dissociation of gases on the electrode surface, and the charges transfer occurring at the boundary between the electrolyte and electrode [54,55], respectively. The results suggest that when LZN$_x$ is used as symmetric cells catalyst, the gas diffusion of ammonia as well as intermediate products may be the rate-determining step. Based on the above analysis and discussion, a schematic diagram of the $NH_3$-SOFCs reaction is proposed with LZN$_x$-YSZ as the anode in Fig. 10.

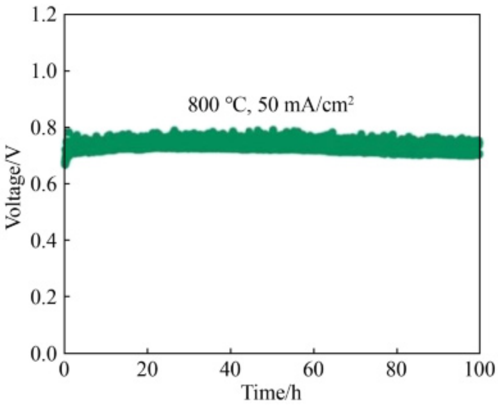

**Fig. 8** Stability of the single cell at 50 mA/cm$^2$ and 800 °C.

## 4 Conclusions

In the present work, $La_2Zr_{2-x}Ni_xO_7$ (LZN$_x$, $x$ = 0, 0.02, 0.05, 0.08, 0.10) pyrochlor oxides are successfully

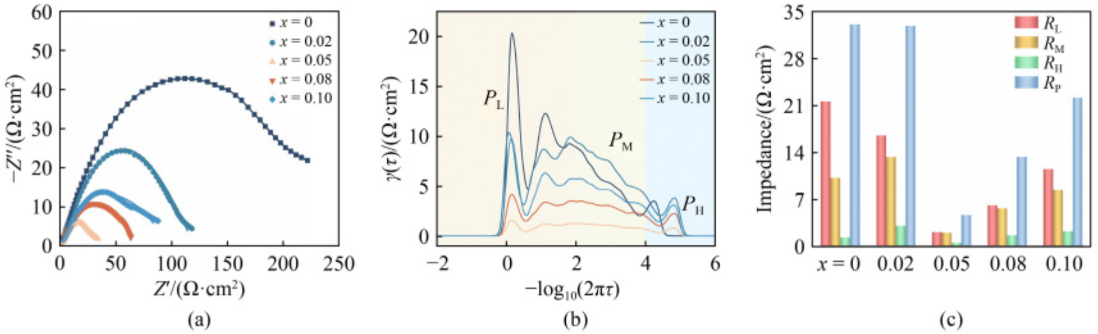

**Fig. 9** DRT analysis.
(a) Nyquist plots; (b) DRT diagrams; (c) $R_L$, $R_M$, $R_H$, and $R_P$ of LZN$_x$-40YSZ|YSZ|LZN$_x$-40YSZ symmetric cell in $NH_3$ at 800 °C.

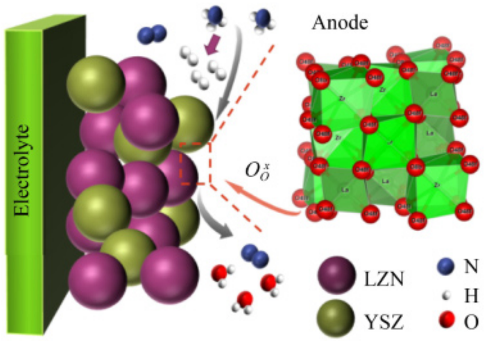

**Fig. 10** Schematic of $NH_3$-SOFCs with $LZN_x$-YSZ as anode.

synthesized, and thoroughly examined as a potential anode catalyst for $NH_3$-SOFCs applications. By employing a combination of various characterization techniques and electrochemical performance assessments, the following results are obtained:

(1) XRD and Raman analyses show that the $LZN_x$ oxide possesses a cubic pyrochlore structure with the Fd-3m space group.

(2) Findings from UV-vis DRS and Mott-Schottky indicate that the $LZN_x$ oxide exhibits an n-type semiconductor behavior. The $E_{CB}$ and bandgap width of the oxide reach the minimum at $x = 0.05$, suggesting that $LZN_{0.05}$ may have a superior electrocatalytic activity.

(3) The results of XRD, SEM, and TEC demonstrate a favorable chemical compatibility between $LZN_x$ pyrochlore oxide and YSZ electrolyte.

(4) The doping of $Ni^{2+}$ effectively improves the conductivity of the material. The conductivity of $LZN_{0.05}$ in $NH_3$ atmosphere is approximately 13 times higher than that of $LZN_0$.

(5) Electrochemical assessments of $LZN_x$-40YSZ anode utilizing $NH_3$ as fuel are conducted, revealing that the maximum power density of the $LZN_{0.05}$-40YSZ anode reaches 100.86 $mW/cm^2$. This value is 1.8 times greater than that of NiO-based $NH_3$-SOFCs (56.75 $mW/cm^2$).

(6) The extended durability assessment indicates that the $NH_3$-SOFCs utilizing the $LZN_{0.05}$-40YSZ composite anode exhibits a negligible voltage degradation following uninterrupted operation at 800 °C under a consistent current density of 50 $mA/cm^2$ for over 100 h.

**Acknowledgements** This work was supported by the National Natural Science Foundation of China (Grant Nos. 22378069, 22278081, and 22308055), the Science Fund for Creative Research Groups of the National Natural Science Foundation of China (Grant No. 22221005), the National Key R&D Program of China (Grant Nos. 2022YFB4003701 and 2022YFB4002404), the Natural Science Foundation of Fujian Province, China (Grant Nos. 2023J01066 and 2022J05027), the Talent Program of Fuzhou University (Grant No. XRC-22036).

**Electronic Supplementary Material** Supplementary material is available in the online version of this article at https://doi.org/10.1007/s11708-024-0948-2 and is accessible for authorized users.

**Competing Interests** The authors declare that they have no competing interets.

## References

1. Ni M, Leung M, Leung Y C. Ammonia-fed solid oxide fuel cells for power generation—A review. International Journal of Energy Research, 2009, 33(11): 943–959
2. Ni M, Leung M, Sumathy K, et al. Potential of renewable hydrogen production for energy supply in Hong Kong. International Journal of Hydrogen Energy, 2006, 31(10): 1401–1412
3. Dodds P E, Staffell I, Hawkes A D, et al. Hydrogen and fuel cell technologies for heating: A review. International Journal of Hydrogen Energy, 2015, 40(5): 2065–2083
4. Estevez R, López-Tenllado F J, Aguado-Deblas L, et al. Current research on green ammonia ($NH_3$) as a potential vector energy for power storage and engine fuels: A review. Energies, 2023, 16(14): 5451–5484
5. Zheng Y, Zhao C, Wu T, et al. Enhanced oxygen reduction kinetics by a porous heterostructured cathode for intermediate temperature solid oxide fuel cells. Energy and AI, 2020, 2: 100027
6. Zhang M, Hashinokuchi M, Yokochi R, et al. Effect of Infiltrated transition metals in Ni/Sm-doped $CeO_2$ cermets anode in direct $NH_3$-fueled SOFCs. ECS Transactions, 2017, 78(1): 1517–1522
7. Jia X, Lu F, Liu K, et al. Improved performance of IT-SOFC by negative thermal expansion $Sm_{0.85}Zn_{0.15}MnO_3$ addition in $Ba_{0.5}Sr_{0.5}Fe_{0.8}Cu_{0.1}Ti_{0.1}O_3$-cathode. Journal of Physics Condensed Matter, 2022, 34(18): 184001
8. Bi L, Fabbri E, Traversa E. Solid oxide fuel cells with proton-conducting $La_{0.99}Ca_{0.01}NbO_4$ electrolyte. Electrochimica Acta, 2018, 260: 748–754
9. Lee J G, Park J H, Shul Y G. Tailoring gadolinium-doped ceria-based solid oxide fuel cells to achieve 2 $W/cm^2$ at 550 °C. Nature Communications, 2014, 5(1): 4045
10. Winter C J. Hydrogen energy—Abundant, efficient, clean: A debate over the energy-system-of-change. International Journal of Hydrogen Energy, 2009, 34(14): S1–S52
11. Song Y, Li H, Xu M, et al. Infiltrated NiCo alloy nanoparticle decorated perovskite oxide: A highly active, stable, and antisintering anode for direct-ammonia solid oxide fuel cells. Small, 2020, 16(28): 2001859
12. Zheng Y , Li Y, Wu T, et al. Controlling crystal orientation in multilayered heterostructures toward high electro-catalytic activity for oxygen reduction reaction. Nano Energy, 2019, 62: 521–529
13. Lu L, Liu Y, Zhang H, et al. Exploring the potential of triple conducting perovskite cathodes for high-performance solid oxide fuel cells: A comprehensive review. Journal of Materials Chemistry. A, Materials for Energy and Sustainability, 2023, 11(44): 23613–23639
14. Jensen J O, Vestbø A P, Li Q, et al. The energy efficiency of onboard hydrogen storage. Journal of Alloys and Compounds, 2007, 446–447: 723–728
15. Li F, Li Y, Chen H, et al. Impact of strain-induced changes in

defect chemistry on catalytic activity of $Nd_2NiO_{4+\delta}$ electrodes. ACS Applied Materials & Interfaces, 2018, 10: 36926–36932

16. Molouk A, Yang J, Okanishi T, et al. Comparative study on ammonia oxidation over Ni-based cermet anodes for solid oxide fuel cells. Journal of Power Sources, 2016, 305: 72–79
17. Hashinokuchi M, Zhang M, Yokochi R, et al. Enhanced activity and stability of Ni-based binary anode in direct $NH_3$-fueled SOFCs. ECS Transactions, 2017, 78(1): 1495–1500
18. Zheng Y, Zhao C, Li Y, et al. Directly visualizing and exploring local heterointerface with high electro-catalytic activity. Nano Energy, 2020, 78: 105236
19. Teramoto K, Iwai H, Kishimoto M, et al. Direct reforming of methane-ammonia mixed fuel on Ni-YSZ anode of solid oxide fuel cells. International Journal of Hydrogen Energy, 2020, 45(15): 8965–8974
20. Li Y, Zhang W, Wu T, et al. Segregation induced self-assembly of highly active perovskite for rapid oxygen reduction reaction. Advanced Energy Materials, 2018: 1801893
21. Fuerte A, Valenzuela R X, Escudero M J, et al. Ammonia as efficient fuel for SOFC. Journal of Power Sources, 2009, 192(1): 170–174
22. Wang W, Su C, Wu Y, et al. Progress in solid oxide fuel cells with nickel-based anodes operating on methane and related fuels. Chemical Reviews, 2013, 113(10): 8104–8151
23. Cao J, Li Y, Zheng Y, et al. A novel solid oxide electrolysis cell with micro-/nano channel anode for electrolysis at ultra-high current density over 5 A/cm$^2$. Advanced Energy Materials, 2022, 12: 2200899
24. Brightman E, Ivey D G, Brett D J L, et al. The effect of current density on $H_2S$-poisoning of nickel-based solid oxide fuel cell anodes. Journal of Power Sources, 2011, 196(17): 7182–7187
25. Molouk A, Yang J, Okanishi T, et al. Electrochemical and catalytic behavior of Ni-based cermet anode for ammonia-fueled SOFCs. ECS Transactions, 2015, 68(1): 2751–2762
26. Kahlenberg V, Böhm H. X-ray diffraction investigation of the defect pyrochlore $Bi_{1.61}Zn_{0.18}Ti_{1.94}V_{0.06}O_{6.62}$. Journal of Alloys and Compounds, 1995, 223(1): 142–146
27. Xu J, Peng L, Fang X, et al. Developing reactive catalysts for low temperature oxidative coupling of methane: On the factors deciding the reaction performance of $Ln_2Ce_2O_7$ with different rare earth A sites. Applied Catalysis A, General, 2018, 552: 117–128
28. Matsumoto M, Aoyama K, Matsubara H, et al. Thermal conductivity and phase stability of plasma sprayed $ZrO_2$-$Y_2O_3$-$La_2O_3$ coatings. Surface and Coatings Technology, 2005, 194(1): 31–35
29. Guo Y, He W, Guo H. Thermal-physical and mechanical properties of $Yb_2O_3$ and $Sc_2O_3$ co-doped $Gd_2Zr_2O_7$ ceramics. Ceramics International, 2020, 46(11): 18888–18894
30. Mizusaki J, Yoshihiro M, Yamauchi S, et al. Nonstoichiometry and defect structure of the perovskite-type oxides $La_{1-x}Sr_xFeO_3$. Journal of Solid State Chemistry, 1985, 58(2): 257–266
31. Shimamura K, Arima T, Idemitsu K, et al. Thermophysical properties of rare-earth-stabilized zirconia and zirconate pyrochlores as surrogates for actinide-doped zirconia. International Journal of Thermophysics, 2007, 28(3): 1074–1084
32. Glerup M, Nielsen O F, Poulsen F W. The structural transformation from the pyrochlore structure $A_2B_2O_7$ to the fluorite structure $AO_2$ studied by Raman spectroscopy and defect chemistry modeling. Journal of Solid State Chemistry, 2001, 160(1): 25–32
33. Mandal B, Krishna P, Tyagi A. Order–disorder transition in the $Nd_{2-y}Y_yZr_2O_7$ system: Probed by X-ray diffraction and Raman spectroscopy. Journal of Solid State Chemistry, 2010, 183(1): 41–45
34. Kong L, Karatchevtseva I, Gregg D J, et al. A novel chemical route to prepare $La_2Zr_2O_7$ pyrochlore. Journal of the American Ceramic Society, 2013, 96(3): 935–941
35. Lü S, Zhu Y, Fu X, et al. A-site deficient Fe-based double perovskite oxides $Pr_xBaFe_2O_{5+\delta}$ as cathodes for solid oxide fuel cells. Journal of Alloys and Compounds, 2022, 911: 165002
36. Feng J, Xiao B, Zhou R, et al. Thermal expansion and conductivity of $RE_2Sn_2O_7$ (RE = La, Nd, Sm, Gd, Er and Yb) pyrochlores. Scripta Materialia, 2013, 69(5): 401–404
37. Fan Q, Zhang F, Wang F, et al. Molecular dynamics calculation of thermal expansion coefficient of a series of rare-earth zirconates. Computational Materials Science, 2009, 46(3): 716–719
38. Miller R A. Thermal barrier coatings for aircraft engines: History and directions. Journal of Thermal Spray Technology, 1997, 6: 35–42
39. Stefaniuk I. Electron paramagnetic resonance study of impurities and point defects in oxide crystals. Opto-Electronics Review, 2018, 26(2): 81–91
40. Wang W, Yang Y, Huan D, et al. An excellent OER electrocatalyst of cubic $SrCoO_{3-\delta}$ prepared by a simple F-doping strategy. Journal of Materials Chemistry. A, Materials for Energy and Sustainability, 2019, 7(20): 12538–12546
41. Araya T, Jia M, Yang J, et al. Resin modified MIL-53 (Fe) MOF for improvement of photocatalytic performance. Applied Catalysis B: Environmental, 2017, 203: 768–777
42. Zhao W, Zhao W, Zhu G, et al. Black strontium titanate nanocrystals of enhanced solar absorption for photocatalysis. CrystEngComm, 2015, 17(39): 7528–7534
43. Wang W, Chen X, Liu G, et al. Monoclinic dibismuth tetraoxide: A new visible-light-driven photocatalyst for environmental remediation. Applied Catalysis B: Environmental, 2015, 176–177: 444–453
44. Yu J C, Yu J, Ho W, et al. Effects of F-doping on the photocatalytic activity and microstructures of nanocrystalline $TiO_2$ powders. Chemistry of Materials, 2002, 14(9): 3808–3816
45. Hasan M, Arshad M, Ali A, et al. Mg and La co-doped ZnNi spinel ferrites for low resistive applications. Materials Research Express, 2018, 6(1): 016302
46. Cherepanov V, Aksenova T, Gavrilova L Y, et al. Structure, nonstoichiometry and thermal expansion of the NdBa $(Co,Fe)_2O_{5+\delta}$ layered perovskite. Solid State Ionics, 2011, 188(1): 53–57
47. Liu H, Yu J. Catalytic performance of Cu-Ni/$La_{0.75}Sr_{0.25}Cr_{0.5}Mn_{0.5}O_{3-\delta}$ for dry methane reforming. International Journal of Energy Research, 2022, 46(8): 10522–10534
48. Kim J H, Manthiram A. $LnBaCo_2O_{5+\delta}$ oxides as cathodes for intermediate-temperature solid oxide fuel cells. Journal of the

Electrochemical Society, 2008, 155(4): B385–B390

49. Miyazaki K, Okanishi T, Muroyama H, et al. Development of Ni-Ba(Zr,Y)$O_3$ cermet anodes for direct ammonia-fueled solid oxide fuel cells. Journal of Power Sources, 2017, 365: 148–154
50. Yang J, Akagi T, Okanishi T, et al. Catalytic influence of oxide component in Ni-based cermet anodes for ammonia-fueled solid oxide fuel cells. Fuel Cells, 2015, 15(2): 390–397
51. Meng G, Jiang C, Ma J, et al. Comparative study on the performance of a SDC-based SOFC fueled by ammonia and hydrogen. Journal of Power Sources, 2007, 173(1): 189–193
52. Wang B, Li T, Gong F, et al. Ammonia as a green energy carrier: Electrochemical synthesis and direct ammonia fuel cell—A comprehensive review. Fuel Processing Technology, 2022, 235: 107380
53. Sharma R K, Burriel M, Dessemond L, et al. Design of interfaces in efficient $Ln_2NiO_{4+\delta}$ (Ln = La, Pr) cathodes for SOFC applications. Journal of Materials Chemistry. A, Materials for Energy and Sustainability, 2016, 4(32): 12451–12462
54. Huang Q A, Hui R, Wang B, et al. A review of AC impedance modeling and validation in SOFC diagnosis. Electrochimica Acta, 2007, 52(28): 8144–8164
55. Bian L, Duan C, Wang L, et al. Electrochemical performance and stability of $La_{0.5}Sr_{0.5}Fe_{0.9}Nb_{0.1}O_{3-\delta}$ symmetric electrode for solid oxide fuel cells. Journal of Power Sources, 2018, 399: 398–405